Hearing Research 304 (2013) 49–56

Contents lists available at SciVerse ScienceDirect

Hearing Research

journal homepage: www.elsevier.com/locate/heares

Research paper

Simultaneous 3D imaging of sound-induced motions of the tympanic membrane and middle ear ossicles

Ernest W. Chang [a,b,1,2,3,4], Jeffrey T. Cheng [c,d,2], Christof Röösli [c,d,e,2], James B. Kobler [f,g,2], John J. Rosowski [c,d,h,**,1,3,4], Seok Hyun Yun [a,h,i,*,1,3,4]

[a] Wellman Center for Photomedicine, Massachusetts General Hospital, 50 Blossom St., Boston, MA 02114, USA
[b] Department of Biomedical Engineering, Boston University, Boston, MA, USA
[c] Eaton-Peabody Laboratory, Massachusetts Eye and Ear Infirmary, Boston, MA, USA
[d] Department of Otology and Laryngology, Harvard Medical School, Boston, MA, USA
[e] Department of Otorhinolaryngology, Head and Neck Surgery, University Hospital Zürich, Switzerland
[f] Department of Surgery, Harvard Medical School, Boston, MA, USA
[g] Center for Laryngeal Surgery and Voice Rehabilitation, Massachusetts General Hospital, MA, USA
[h] Harvard-MIT Health Science and Technology, Cambridge, MA, USA
[i] Department of Dermatology, Harvard Medical School, Boston, MA, USA

ARTICLE INFO

Article history:
Received 3 April 2013
Received in revised form
10 June 2013
Accepted 16 June 2013
Available online 28 June 2013

ABSTRACT

Efficient transfer of sound by the middle ear ossicles is essential for hearing. Various pathologies can impede the transmission of sound and thereby cause conductive hearing loss. Differential diagnosis of ossicular disorders can be challenging since the ossicles are normally hidden behind the tympanic membrane (TM). Here we describe the use of a technique termed optical coherence tomography (OCT) vibrography to view the sound-induced motion of the TM and ossicles simultaneously. With this method, we were able to capture three-dimensional motion of the intact TM and ossicles of the chinchilla ear with nanometer-scale sensitivity at sound frequencies from 0.5 to 5 kHz. The vibration patterns of the TM were complex and highly frequency dependent with mean amplitudes of 70–120 nm at 100 dB sound pressure level. The TM motion was only marginally sensitive to stapes fixation and incus-stapes joint interruption; however, when additional information derived from the simultaneous measurement of ossicular motion was added, it was possible to clearly distinguish these different simulated pathologies. The technique may be applicable to clinical diagnosis in Otology and to basic research in audition and acoustics.

The tympanic membrane (TM) and the middle ear ossicles (malleus, incus and stapes) play a pivotal role in hearing by gathering and transmitting airborne sound waves to the cochlea. In the most sensitive frequency range, between 1 and 5 kHz, a normal human can detect sound pressure levels (SPL) as low as 20 μP (0 dB SPL), corresponding to TM vibration amplitudes of less than 10 pm (Merchant and Rosowski, 2010). Conversational speech (40–60 dB SPL) produces motions that are 10–100 fold larger. Middle-ear injuries (e.g. perforations of the TM or dislocation of the ossicles) or disease (e.g. otosclerosis causing joint fixation) can attenuate sound conduction by as much as 50–60 dB, seriously compromising communication.

It is estimated that worldwide over 12 million adults have moderate to severe conductive hearing loss (Holley, 2005). In current clinical practice, no diagnostic methods can reliably and noninvasively differentiate between different ossicular disorders. Otoscopy is commonly used to determine the presence of middle-ear infection and perforations of the TM. However, ossicular disorders are not visible through the intact TM. Standard audiometry quantifies the degree of conductive hearing loss, but it cannot provide a differential diagnosis. Tympanometry, which measures acoustic reflections from the whole TM at different static pressures,

* Corresponding author. Wellman Center for Photomedicine, Massachusetts General Hospital, 65 Landsdowne St. UP-525, Cambridge, MA 02139, USA. Tel.: +1 617 768 8704.
** Corresponding author. Eaton-Peabody Laboratory, Massachusetts Eye and Ear Infirmary, Boston, MA, USA.
E-mail addresses: John_Rosowski@meei.harvard.edu (J.J. Rosowski), syun@hms.harvard.edu (S.H. Yun).

[1] E.W.C., J.J.R., and S.H.Y designed research.
[2] E.W.C., J.T.C., C.R., J.B.K performed research.
[3] E.W.C., J.J.R., S.H.Y. analyzed data.
[4] E.W.C., J.J.R., and S.H.Y. wrote the paper.

0378-5955/$ – see front matter © 2013 Elsevier B.V. All rights reserved.
http://dx.doi.org/10.1016/j.heares.2013.06.006

allows a diagnosis of middle-ear fluid (Dempster and Mackenzie, 1991), but cannot reliably differentiate ossicular pathologies because of the variability in the coupling of the TM to the ossicles (Jerger, 1975; Nakajima et al., 2012; Shanks and Schohet, 2009). Presently, the definitive diagnosis of ossicular pathologies requires invasive surgical exploration that involves incising the TM around its periphery and lifting the TM to expose the ossicles (Athanasiadis-Sismanis and Poe, 2010). A noninvasive method capable of identifying the cause of conductive hearing loss without having to lift the TM would be highly useful for differential diagnosis and to improve the pre-surgical planning and outcomes of ossicular reconstructive procedures (Fisch et al., 2001; Rosowski et al., 2008).

Scanning laser vibrometry (LDV) (Huber et al., 2001; Rosowski et al., 2008) and laser holography (Cheng et al., 2010; Rosowski et al., 2009; Wada et al., 2002) provide quantitative information about the amplitude and phase of vibration. However, these methods are surface measurements and therefore require invasive surgical procedures to access the incus and stapes (Chien et al., 2009). In contrast, optical coherence tomography (OCT) with infrared light can penetrate tissues and provide cross-sectional imaging at various depths (Heermann et al., 2002; Just et al., 2009; Lin et al., 2008; Pitris et al., 2001). While use of OCT for retinal imaging is valuable and widespread, applications to hearing, where tissues may be in vibratory motion, have just begun to be explored. OCT has recently been used to measure the vibrational amplitudes produced by 0.5 kHz stimulation of the malleus and incus through the TM in cadaveric human ears (Subhash et al., 2012) and motion of the Organ of Corti in guinea pigs has been measured through the round window (Chen et al., 2011).

In this paper, we describe a novel technique termed OCT vibrography that simultaneously captures the three-dimensional shape and sound-induced motion of the TM and substantial parts of the ossicular chain with high spatial and dynamic resolution. The vibrography system uses synchronized data acquisition, beam scanning and sound stimulus generation (Chang et al., 2012). We tested the system on cadaver chinchilla temporal bones at frequencies ranging from 0.5 to 5 kHz. Surgical models of ossicular fixation and dislocation were used to assess the potential of the method to detect and differentiate various pathologies in the middle ear.

1. Methods

1.1. Imaging system

The OCT system employed a wavelength-swept laser source with a tuning range from 1220 to 1350 nm and an average output power of 30 mW at the sample (Yun et al., 2003, 2006). The laser was operated at a sweeping repetition rate between 15 and 20 kHz. The sample arm employed a pair of XY galvanometer-mounted mirror scanners (Cambridge Technologies) and a 35 mm focusing lens. The focus of the infrared laser light was placed approximately at the mid-plane of the middle ear space between the TM and cochlear wall. The system controlled a loudspeaker (Auvio 3-way speaker) to generate pure tone sound stimuli and synchronously measured the amplitude and phase of the light scattered from middle-ear tissues (Fig. 1a and Fig. S1). Monotone sinusoidal signals from a synthesizer were amplified with an audio amplifier and directed to the loudspeaker placed above the specimen (Figs. S2). A calibrated probe microphone was placed near the edge of the TM to record the sound pressure level (SPL) applied to the TM surface. A two-channel 10 MS/s data acquisition board (National Instruments) was used to acquire the interferometric signals. A single clock generated from the data acquisition board served as a master clock that synchronized the XY galvanometers and loudspeaker with the laser sweeps. The transverse and axial resolutions of the OCT system were 25 and 12 μm, respectively.

1.2. Vibrography data acquisition

At a given position of the optical beam, a series of axial lines (A-lines), locked in time to selected phases of the acoustic stimulus, were acquired during a single (or a few) cycle(s) of sound stimulation. The scanning mirrors steered the OCT beam to measure reflectance from a column of 500 points along an A-line (z-axis) at a specific XY grid locations. After this was repeated for one cycle, the beam was moved to a neighboring location, and a new series of A-lines was gathered. Repeating this step, the probe beam was scanned laterally across the sample to acquire four-dimensional data containing the amplitude and phase of the scattered light at three-dimensional spatial coordinates (x, y, z) as a function of time or motion phase (φ) (Fig. S3). The number of motion phases acquired per cycle was determined by the ratio of the A-line rate and

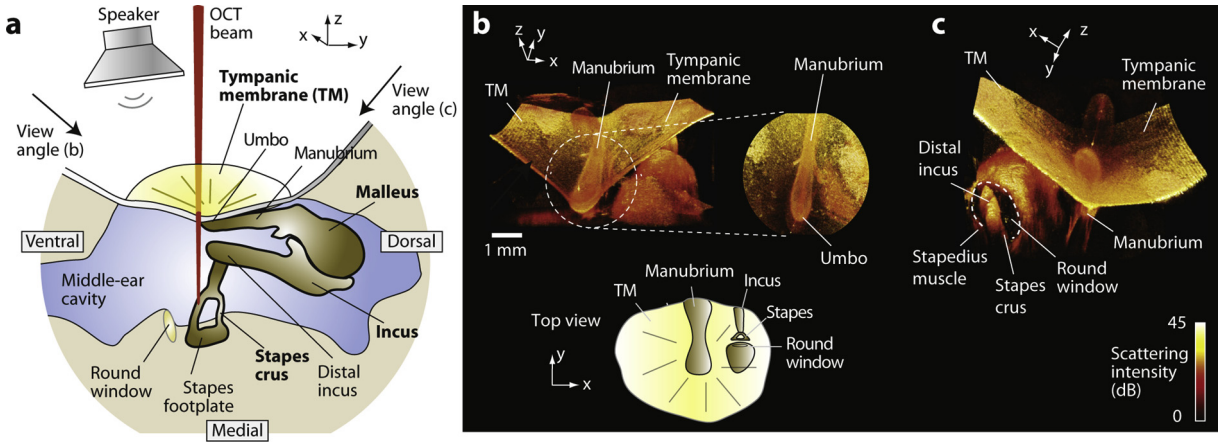

Fig. 1. Views of ear anatomy. (a) A schematic representation of the TM and the middle ear. (b) 3D OCT images of the chinchilla middle ear. The view angle of rendering is indicated in (a). The left figure shows a fraction of the TM surface as well as some of the structure medial to the TM looking from ventral to dorsal. The manubrium of the malleus is oriented along the ventral–dorsal projection ($-y$ to $+y$). Positive x is anterior. The expanded view shows the manubrium in the center of the TM and umbo near the bottom. The bottom inset is a schematic of corresponding anatomy (top view). (c) A view looking from dorsal to ventral, as indicated in (a). The image shows the round window in the cochlear base, a segment of the distal incus (the ventral most projection of the incus), and one crus of the stapes. The prong-like structures below the manubrium are shadows in the reconstruction.

vibration frequency. For example, for an A-line rate of 18,000 Hz and sound frequency of 1500 Hz, 12 (=18,000/1500) motion phases were captured (Kobler et al., 2010). A subsequent binning of the acquired data with respect to the motion phase generated a series of "snapshot" images over the vibration cycle. To cancel inherent deterministic motion jitter from the scanner and normalize the measurements for deterministic sound-induced bulk motion of the specimen, a reference measurement was made on a quasi-stationary object within the scan volume (usually the bony wall of the cochlea). The measured jitter was then subtracted from all measurements. The sensitivity to vibration amplitude, which depends on the magnitude of light scattering, was about 0.5 nm for the TM and about 5 nm for the stapes (where the reflected signal was more attenuated). For more details of data processing, see Supplementary Information.

1.3. Tissue preparation

Three cadaver chinchillas were used. The cartilaginous and bony external ear canals were removed from the 3 chinchilla specimens to expose most of the TM while maintaining the integrity of the bony TM annulus. The middle ear was maintained widely open to allow surgical manipulation of the ossicular chain. Stapes immobilization was achieved by applying a drop of cyanoacrylic cement between the stapes footplate and surrounding bone. A surgical hook was used to interrupt the incudo-stapedial joint. In one case we also removed one crus of the stapes. The cadaveric specimens were kept moist between measurements by applying saline.

2. Results

2.1. Optical coherence vibrography of the chinchilla middle ear

In the chinchilla ear, the superior (dorsal) malleus head and incus body are obscured by the opaque bony structures around the TM (Fig. 1a). However, the manubrium (the handle of the malleus embedded in the TM) and parts of the incus, stapes and cochlear wall are readily visualized. Fig. 1b shows representative renderings of the imaged volume (7 mm × 7 mm × 3 mm in *xyz*). The images show the topography of the intact, cone-shaped TM, the manubrium, the umbo near the center of the TM, the inferior or distal portion of the incus, the lateral portion of the stapes crura, the tendon of the stapedius muscle, and a partial view of the cochlea including the bone surrounding the round window (Vrettakos et al., 1988).

2.2. Digitally reconstructed snapshot vibrational images

Vibrography produced a series of images corresponding to evenly spaced phases (φs) of motion over one vibratory cycle (Fig. S5). A large number of cycles were used to create the final sequence since each cycle contributes a single axial line in each image. The number of phases equals the A-line acquisition rate (15–20 kHz) divided by the sound frequency (0.5–5 kHz). In these experiments the number of phases ranged from 4 to 30. The displacement in *z* was visualized using a standard color map overlaid on the structural images (Fig. S6, Videos S1, S2).

Supplementary data related to this article can be found online at http://dx.doi.org/10.1016/j.heares.2013.06.006.

Fig. 2a shows a top view of the exposed chinchilla ear, and Fig. 2b shows the corresponding vibration pattern at the maximum overall upward displacement of the TM. The sound frequency was 1525 Hz, with an SPL of 104 dB. With these stimulus parameters the pattern of vibration of the TM was complex. The TM was next digitally segmented and removed to view motion of the underlying ossicles (Fig. 2c). The manubrium, distal incus and the head of the stapes were clearly visible (Fig. 2d). Fig. 2e shows corresponding vibrography images at two phases where there were maximal inward (positive) and outward (negative) displacements of the umbo. The images show an amplitude gradient along the manubrium, and in-phase motion of the manubrium, distal incus, and stapes. The tympanic ring and cochlea also show a relatively small amount of motion to the intense stimulus. The 3D dataset allows the ossicular chain to be viewed from different angles. In Fig. 2f, a portion of the distal incus was digitally removed to view the most ventral portion of the incus, the posterior and anterior crura of the stapes, the petrous bone surrounding the round window, and the fluid-filled scala tympani of the cochlea. The ventral incus, stapes crura, and stapes footplate were observed to vibrate nearly in phase. The vibration of the round window membrane may also be detectable as small spots in the round window area that changed from pale green to light blue in opposite phase to stapes motion. The sound-induced motion of ossicles was also visualized by digitally exaggerating the motion (Fig. 2g and Video S3).

Supplementary data related to this article can be found online at http://dx.doi.org/10.1016/j.heares.2013.06.006.

2.3. Vibration of the TM at various frequencies

Fig. 3a shows amplitude and phase maps of the TM for the stimuli of near 100 dB SPL at 800, 1910, and 3050 Hz. As expected, the number and complexity of the vibration modes increased with frequency. At 800 Hz the entire TM moved relatively in-phase, while at 1910 Hz and 3050 Hz there were multiple sharply defined nodes as well as more gradual phase transitions that suggest either the presence of traveling waves or damped modal motions on the TM surface. The root-mean-square (RMS) amplitude, averaged over the TM surface, was approximately 170 nm at 800 Hz (104 dB), 85 nm at 1910 Hz (102 dB), and 75 nm at 3050 Hz (96 dB). From the series of vibrography images, the average displacement over the TM surface was calculated. Assuming a typical area of 60 mm^2 for the chinchilla TM, the RMS volume displacements of the TM normalized by the sound pressure were calculated to be 2×10^{-3}, 0.3×10^{-3}, and 1×10^{-3} mm^3/Pa for 800, 1910, and 3050 Hz, respectively.

2.4. Effects of simulated ossicular disorders on TM motion

To investigate the potential of this method for identifying middle ear pathologies that would affect the relative motion of the TM and ossicles, we simulated two prevalent disorders: otosclerosis and ossicular joint interruption (Nakajima et al., 2005a,b). Clinically, otosclerosis is an inflammatory process that produces abnormal bony growth of the cochlear wall invading the stapes footplate and impeding its motion. This condition was simulated by immobilizing the stapes footplate with cyanoacrylic glue. Joint interruption was produced using a surgical hook. Fig. 4 shows vibrography images of the TM (top view) before and after the fixation of the stapes and then following interruption of the incudo-stapedial (I–S) joint at 1525 Hz frequency and SPL of 104 dB (See also Videos S4a–c). While the vibration patterns of the TM changed after ossicular manipulations, we failed to draw simple relationships between the TM motion and specific ossicular disorders over the 0.5–5 kHz frequency range tested. For example, the RMS vibration amplitudes of the TM are altered by stapes fixation or joint interruption, but these values were frequency dependent (Fig. S7) and the differences between ossicular disorders were not statistically significant.

Supplementary data related to this article can be found online at http://dx.doi.org/10.1016/j.heares.2013.06.006.

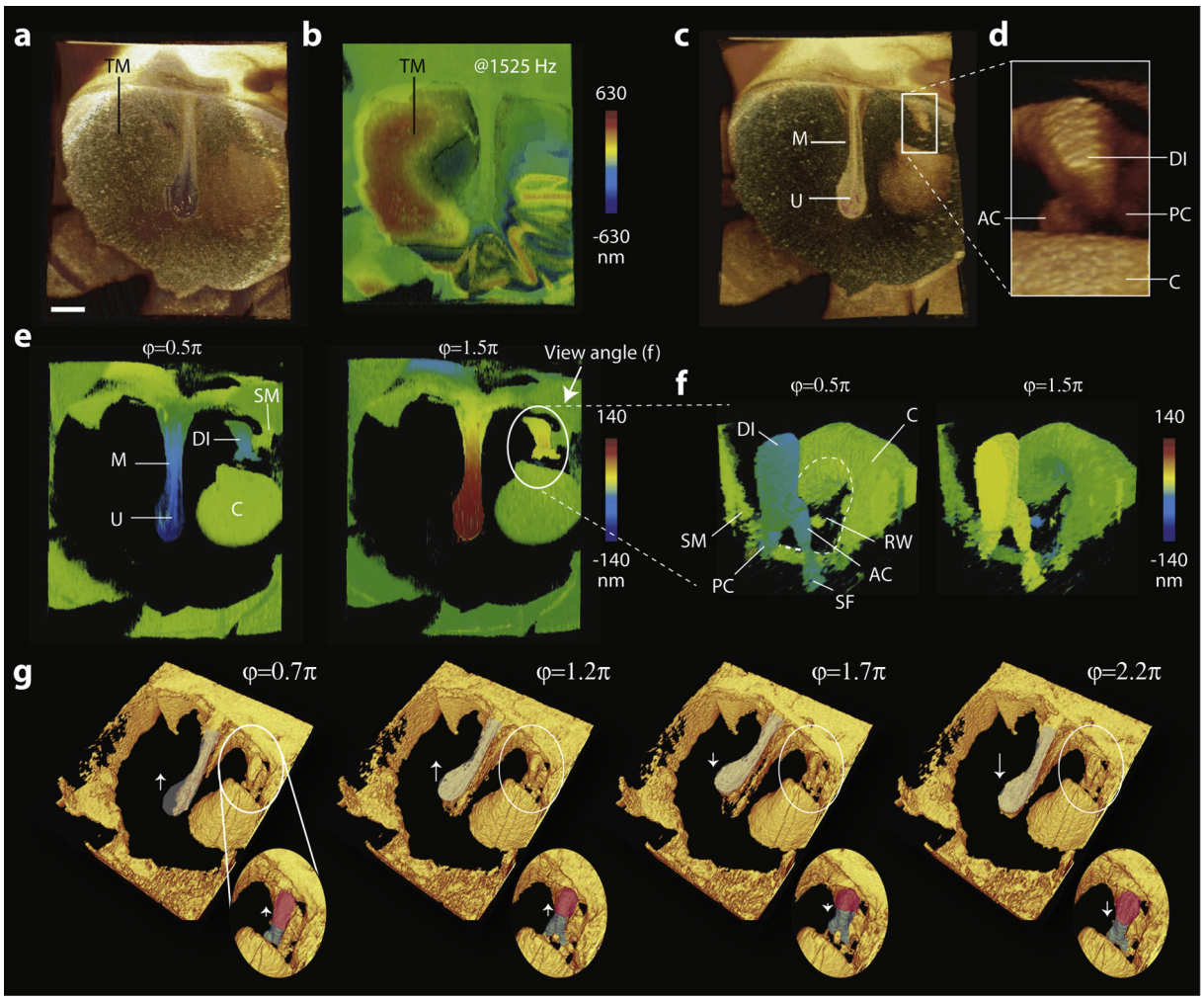

Fig. 2. Structural and functional imaging of the chinchilla ear. (a) Structural image, and (b) a color-coded instantaneous vibrographic map of the outer surface of the TM for stimulation of a 1525 Hz, 104 dB SPL tone. The motions are relative to the position in the no-stimulus condition. (c–e) A view of the middle ear after digital subtraction of the TM. (c) Structural image showing the manubrium (M) of the malleus and the umbo (U). (d) A magnified and slightly rotated view of the cochlear base (C), the distal incus (DI) and the anterior and posterior crura of the stapes (AC & PC). (e) Vibrographic maps at two phases of the tonal stimulus that are one-half-cycle apart. (f) Vibrographic maps of the stapes and incus at the corresponding phases. The view angle from dorsal to ventral is indicated in (e). The vertical motion of the distal incus (DI) and stapes crura (AC and PC) are of similar magnitude at both phases. There are small islands of reflected light that appear to move out of phase with the ossicles. The location of these islands is consistent with the location of the round window membrane. (g) Reconstructions of the computationally 500× magnified motion of the manubrium, incus, and stapes at four phases of vibration. (For interpretation of the references to color in this figure legend, the reader is referred to the web version of this article.)

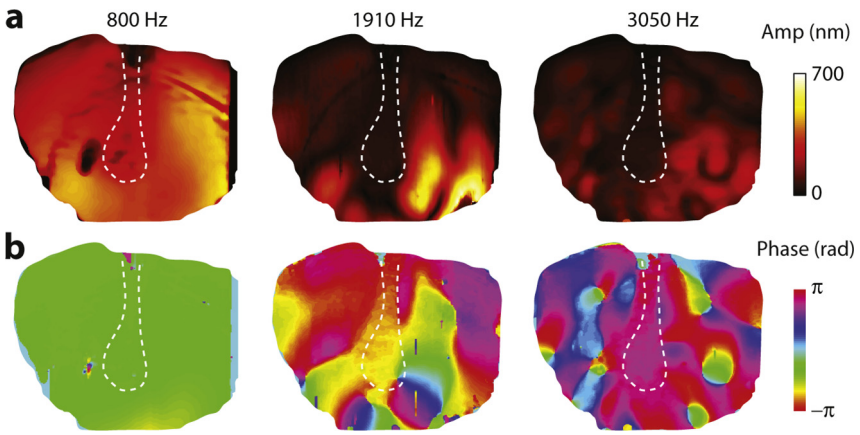

Fig. 3. Vibrographs of the magnitude (a) and phase (b) of the motions of the lateral surface of the TM at three frequencies and SPL levels: 800 Hz and 104 dB, 1910 Hz and 102 dB, and 3050 Hz and 96 dB. Dotted lines, outline of the manubrium.

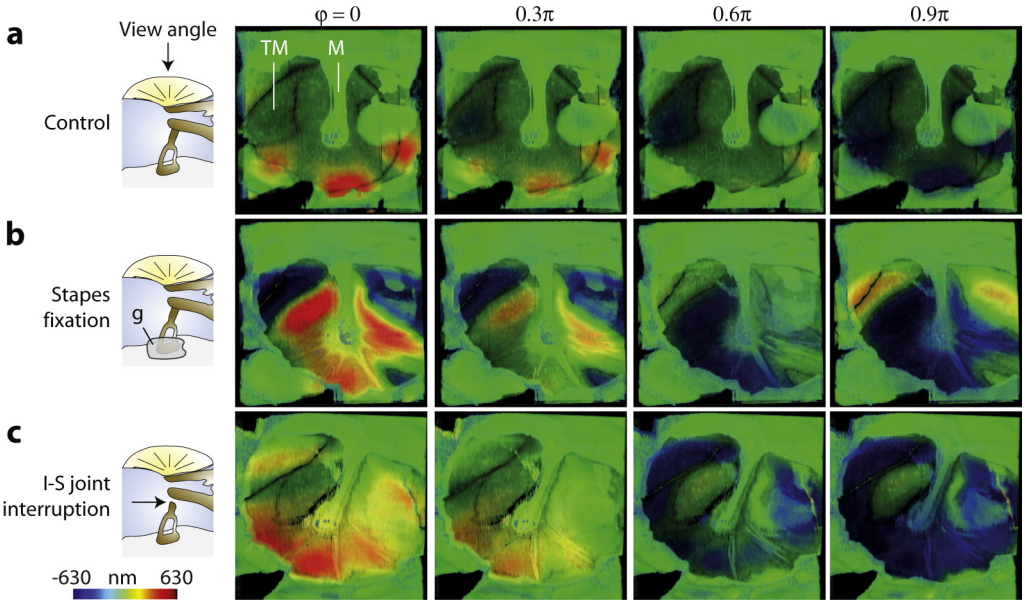

Fig. 4. The effects of ossicular manipulations on the motion of the lateral surface of the TM. For each schematized measurement condition, the images show the position of the TM surface relative to the rest position at four motion phases of 0, 0.3, 0.6 and 0.9π, respectively. The stimulus was a 1525 Hz, 104 dB SPL tone. (a) The control case with intact ossicular chain and mobile stapes. (b) After stapes fixation with cyanoacrylic glue. (c) After interrupting the I–S joint.

2.5. Effects of simulated ossicular disorders on mallear motion

The part of the malleus attached to the TM is the manubrium and the distal, spoon-like tip of the manubrium near the center of the TM is the umbo. The manubrium joins the lateral process of the malleus (LPM) near the edge of the TM. The manubrium is relatively thin near the umbo and thickens toward the LPM. The vibration amplitude of the manubrium was highest at the umbo and decreased toward the LPM (see Fig. 2e). In the normal control state, the entire manubrium oscillated nearly in phase at 1525 Hz (104 dB SPL) (Fig. 5a and b) and at other frequencies up to 5 kHz. This is consistent with simple lever-action of the manubrium with a fulcrum dorsal to the LPM. Stapes fixation decreased the amplitude of manubrial motion and introduced a phase gradient along the length of the manubrium (Fig. 5c and d). Interruption of the I–S joint led to an increase in the vibration amplitude of the entire manubrium above that of the control condition, with a phase of vibration that was largely uniform across the manubrium but slightly lagging with respect to the control (Fig. 5e and f).

2.6. Effects of simulated ossicular disorders on incus and stapes motion

In the control condition, the incus and stapes vibrated with similar magnitudes of 50 nm (1525 Hz, 104 dB) (Fig. 6a and b and Video S5a), and the incus-to-umbo (I–U) and stapes-to-umbo (S–U) amplitude ratios were measured to be about 0.3 (Fig. 6c). When the stapes footplate was fixed, the motion of the incus and the stapes head were reduced from 50 nm to 3 nm (a 24 dB loss; Fig. 6d and e and Video S5b), while the umbo motion was reduced from 120 nm to 20 nm (a 16 dB loss). Stapes fixation reduced both I–U and S–U ratios significantly in a frequency dependent manner ($P < 0.005$) (Fig. 6f). When the I–S joint was interrupted, stapes motion was reduced to the same low-level motion as the cochlear wall (Fig. 6g and Video S5c). In contrast, incus motion increased to 80 nm (4 dB above control), and umbo motion increased to 210 nm (5 dB above control, Fig. 6h). Thus with I–S joint interruption, the S–U ratio was significantly reduced ($P < 0.005$) and I–U ratio was increased ($P < 0.01$) (Fig. 6i).

Supplementary data related to this article can be found online at http://dx.doi.org/10.1016/j.heares.2013.06.006.

2.7. Lissajous visuatlization

Lissajous plots were useful for visualizing the effects of ossicular manipulations on the relative phase of motion of the three ossicles. A Lissajous plot of the relative motions of the incus and the stapes with respect to the umbo traces a highly eccentric ellipse, indicating a small phase lag (delay) between the distal incus and umbo (Fig. 7a) (Ravicz et al., 2010). After stapes fixation, this Lissajous plot became less eccentric (more round) with clockwise rotation (Fig. 7c). This indicates that the motion of both the incus and stapes were now leading the umbo. With the stapes decoupled from the ossicular chain, the Lissajous plot between the incus and umbo become a straight line without a phase lag (Fig. 7c). The stapes versus umbo plot exhibits a highly eccentric ellipse with an apparent $\pi/2$ phase advance.

3. Discussion

We showed that OCT vibrography could simultaneous resolve both the structure and motion of the TM and parts of the ossicular chain. Therefore, this technique should be highly useful for investigating how sound energy is coupled from the TM to the ossicular system in normal and diseased ears (Tuck-Lee et al., 2008).

The observed TM vibration patterns at various sound frequencies were consistent with observations made by laser holography (Cheng et al., 2013; Rosowski et al., 2009, 2013). Several models of the TM emphasize the modal (standing wave) motion of the TM (Funnell, 1983), while other models assume that only the waves traveling along the TM surface are important to ossicular coupling (Goll and Dalhoff, 2011; Parent and Allen, 2010). Consistent with holographic measurements (Cheng et al., 2010, 2013), OCT vibrography images revealed spatial variations in the motion of the TM surface that are consistent with the presence of both modal motions and traveling

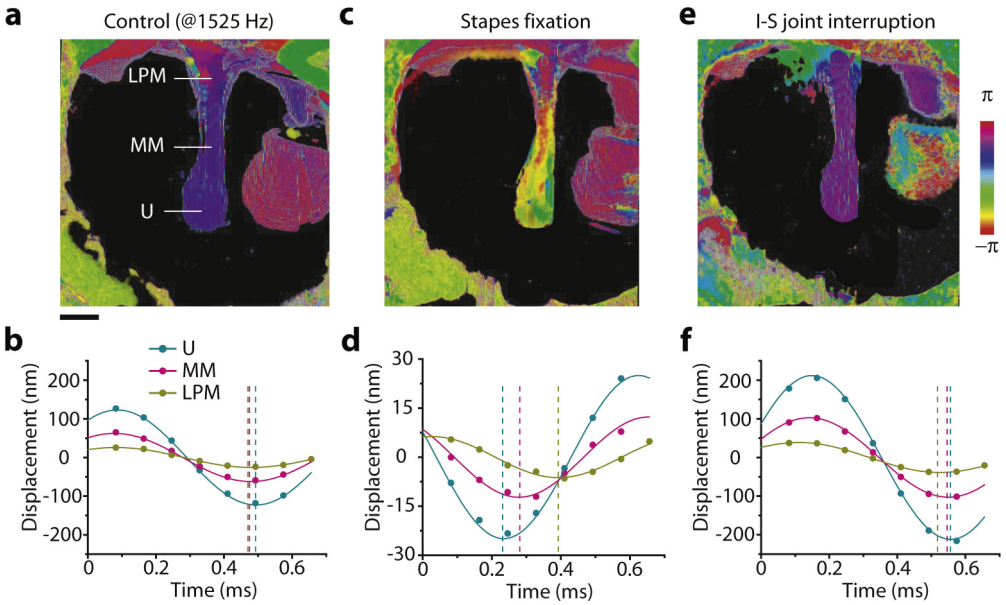

Fig. 5. Magnitude and phase of the motion of the manubrium in the control (a, b), stapes-fixed (c, d) and I–S ioint-interrupted (e, f) conditions. The stimulus was a 1525 Hz, 104 dB SPL tone. (a, c & e) Vibrographic maps showing the phase of motion measured along the lateral surface of the manubrium of the malleus: (U) umbo, (MM) a mid-manubrium position, (LPM) the lateral (dorsal most process) process of the manubrium. (b, d & f) Time waveforms of the motion of the three manubrial locations.

waves. Further analysis in conjunction with measures of ossicular motion may provide new insight into this issue.

Perhaps most significantly, the simultaneous capture of TM and ossicular motion offers novel diagnostic opportunities. The large variation in the sound-induced motion of the TM alone in normal-hearing humans has precluded diagnosis of ossicular problems based solely on TM measures (Nakajima et al., 2012; Rosowski et al., 2008). OCT vibrography increases the diagnostic information available for detecting and discriminating different ossicular disorders, which it may be possible to boil down to some simple clinical metrics. Stapes fixation reduces the motion of all three ossicles and incus-to-umbo and the stapes-to-umbo amplitude ratios (Figs. 5–7). There is also a reversal of the phase relationship between the umbo and the other ossicles. For I–S joint interruption stapes motion is greatly decreased, while umbo and incus motions are increased. Phase relations change such that the incus and umbo

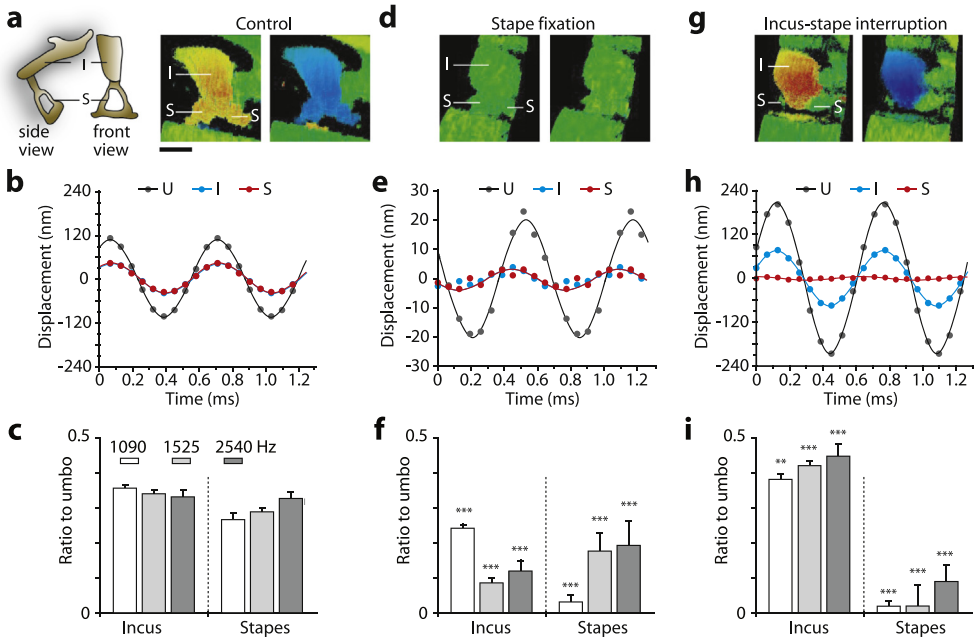

Fig. 6. Vibrographic measurements of the magnitude and phase of the motion of the umbo, incus and stapes in the control (a–c), stapes-fixed (d–f) and I–S joint-interrupted (g–i) conditions. The stimulus was a 1525 Hz, 104 dB SPL tone. (a, d & g) Vibrographic maps showing the displacement relative to rest condition of the incus and stapes. The views are not precisely the same in the three conditions, and the stapes crura are most distinguishable in the control state. (b, e & h) Time waveforms of the displacement of the umbo, incus and stapes in the three conditions. (c, f & i) Measurements of the ratio of the displacement amplitudes of the incus and stapes to the displacement amplitude of the umbo in the three conditions at three frequencies: 1,090, 1,525, and 2540 Hz. The amplitudes were captured at the umbo, the distal portion of incus and from one stapes crus. Error bars represent standard deviation over multiple ($N > 20$) measurements made at adjacent locations. *P*-values (two-sided *t* test) were calculated with respect to the control: ***, <0.005, **, <0.01.

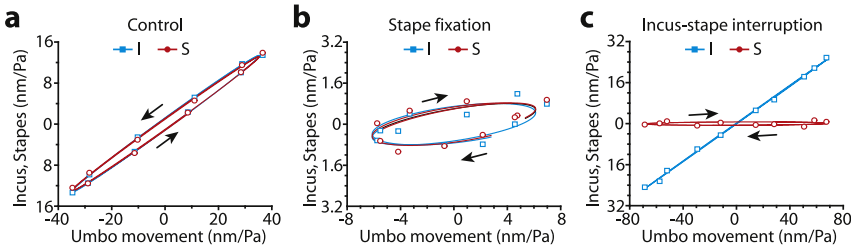

Fig. 7. Lissajous curves of the motion of the incus and stapes relative to that of the umbo in the control (a), stapes-fixed (b) and I–S ioint-interrupted (c) conditions. The stimulus was a 1525 Hz, 104 dB SPL tone.

move in-phase rather than the incus lagging the umbo. Other types of disorders, such as fixation of malleus and incus or interruption of malleus–incus joint, are expected to produce different characteristic alterations in the amplitude and phase responses of the ossicles (Nakajima et al., 2005b).

Some features of middle ear function may be more difficult to image in humans than in chinchilla. For example, in chinchilla we observed the opposite-phased motions of the round window membrane through the TM, a motion that will be more difficult to see in humans with its partially sequestered round window. The greater thickness of the human TM may also reduce the measurement sensitivity of ossicular motion, particularly if the TM is inflamed.

An additional issue in the translation of these findings to the otology clinic is the time required to acquire vibrography images. Measurement duration depends on the sampling resolution in *xy* and is also proportional to the inverse of the frequency of the sound. In our experiments, the 3-dimensional OCT images typically consisted of 500 × 500 × 250 pixels in *x*, *y*, and *z*. With the current system operated at an A-line rate of 20 kHz, 12.5 s are needed per motion phase. Thus at 2 kHz, ten volumetric vibrography images per stimulus cycle can be acquired in about 2 min. This measurement time is acceptable for *ex vivo* studies or preclinical experiments with anesthetized animals, but in a clinic it would be highly desirable for stability and patient comfort reasons to shorten the acquisition time. One strategy would be to reduce the number of *x* and *y* scan points. OCT systems with A-line rates of 400–1000 kHz are also becoming readily available (Klein et al., 2011; Oh et al., 2010).

Since OCT measures back-scattered light, only the motion parallel to the optical beam is measured. As a result, the vibrography measurement underestimates the true vibration amplitude by the cosine of the angle between the optical beam and actual vibrational axis. This error (e.g. 14% for an angular mismatch of 30°) would likely be tolerable for diagnostic applications. Greater accuracy could be achieved using multiple probe beams at different view angles to determine full 3D vector components, including the transverse and shear movements (Ahn et al., 2007; Makita et al., 2008). This enhancement would be useful in measuring the degree of bending and rocking of the ossicles (or prostheses) and the significance of such motions in hearing (Huber and Eiber, 2011).

A clinical instrument can be imagined where TM and middle ear vibrography is performed via the ear canal using a flexible fiber-optic catheter (Nguyen et al., 2012; Yun et al., 2006) or a small-diameter endoscope (Kim et al., 2010), in conjunction with an earphone. With continued development, OCT vibrography should prove useful in basic research, preclinical and clinical settings for noninvasively evaluating the structure and function of the TM and middle ear ossicles.

Acknowledgments

This work was supported by the Center for Biomedical OCT Research and Translation funded by National Institute of Health (P41EB015903, R01DC00194). E.W.C. acknowledges the Wellman Center Graduate Student Scholarship.

Appendix A. Supplementary data

Supplementary data related to this article can be found at http://dx.doi.org/10.1016/j.heares.2013.06.006.

References

Ahn, Y.-C., Jung, W., Chen, Z., 2007. Quantification of a three-dimensional velocity vector using spectral-domain Doppler optical coherence tomography. Optics Letters 32, 1587–1589.
Athanasiadis-Sismanis, A., Poe, D.S., 2010. Ossicular chain reconstruction. In: Gulya, A.J., Minor, L.B., Poe, D. (Eds.), Glasscock-Shambaugh Surgery of the Ear. Shelton, Ct., People's Medical Publishing House, USA, pp. 489–500.
Chang, E.W., Kobler, J.B., Yun, S.H., 2012. Subnanometer optical coherence tomographic vibrography. Optics Letters 37, 3678–3680.
Chen, F.Y., Zha, D.J., Fridberger, A., Zheng, J.F., Choudhury, N., Jacques, S.L., Wang, R.K., Shi, X.R., Nuttall, A.L., 2011. A differentially amplified motion in the ear for near-threshold sound detection. Nature Neuroscience 14, 770–U366.
Cheng, J.T., Aarnisalo, A.A., Harrington, E., Hernandez-Montes, M.D., Furlong, C., Merchant, S.N., Rosowski, J.J., 2010. Motion of the surface of the human tympanic membrane measured with stroboscopic holography. Hearing Research 263, 66–77.
Cheng, J.T., Hamade, M., Harrington, E., Furlong, C., Merchant, S.N., Rosowski, J.J., 2013. Wave motion on the surface of the human tympanic membrane: holographic measurement and modeling analysis. Journal of the Acoustic Society of America 133, 918–937.
Chien, W., Rosowski, J.J., Ravicz, M.E., Rauch, S.D., Smullen, J., Merchant, S.N., 2009. Measurements of stapes velocity in live human ears. Hearing Research 249, 54–61.
Dempster, J.H., Mackenzie, K., 1991. Tympanometry in the detection of hearing impairments associated with otitis-media with effusion. Clinical Otolaryngology 16, 157–159.
Fisch, U., Acar, G.O., Huber, A.M., 2001. Malleostapedotomy in revision surgery for otosclerosis. Otology & Neurotology 22, 776–785.
Funnell, W.R.J., 1983. On the undamped natural frequencies and mode shapes of a finite-element model of the cat eardrum. Journal of the Acoustical Society of America 73, 1657–1661.
Goll, E., Dalhoff, E., 2011. Modeling the eardrum as a string with distributed force. Journal of the Acoustical Society of America 130, 1452–1462.
Heermann, R., Hauger, C., Issing, P.R., Lenarz, T., 2002. Application of optical coherence tomography (OCT) in middle ear surgery. Laryngo-Rhino-Otologie 81, 400–405.
Holley, M.C., 2005. The auditory system, hearing loss and potential targets for drug development. Drug Discovery Today 10, 1269–1282.
Huber, A.M., Eiber, A., 2011. Vibration properties of the ossicle and cochlea and their importance for our hearing system. Hno 59, 255–260.
Huber, A.M., Schwab, C., Linder, T., Stoeckli, S.J., Ferrazzini, M., Dillier, N., Fisch, U., 2001. Evaluation of eardrum laser Doppler interferometry as a diagnostic tool. Laryngoscope 111, 501–507.
Jerger, J., 1975. Impedance terminology. Archives of Otolaryngology-Head & Neck Surgery 101, 589–590.
Just, T., Lankenau, E., Huttmann, G., Pau, H.W., 2009. Optical coherence tomography in middle ear surgery. Hno 57, 421–427.
Kim, P., Chung, E., Yamashita, H., Hung, K.E., Mizoguchi, A., Kucherlapati, R., Fukumura, D., Jain, R.K., Yun, S.H., 2010. In vivo wide-area cellular imaging by side-view endomicroscopy. Nature Methods 7, 303–305.
Klein, T., Wieser, W., Eigenwillig, C.M., Biedermann, B.R., Huber, R., 2011. Megahertz OCT for ultrawide-field retinal imaging with a 1050nm Fourier domain mode-locked laser. Optics Express 19, 3044–3062.
Kobler, J.B., Chang, E.W., Zeitels, S.M., Yun, S.H., 2010. Dynamic imaging of vocal fold oscillation with four-dimensional optical coherence tomography. Laryngoscope 120, 1354–1362.

Lin, J., Staecker, H., Jafri, M.S., 2008. Optical coherence tomography imaging of the inner ear: a feasibility study with implications for cochlear implantation. Annals of Otology Rhinology and Laryngology 117, 341–346.

Makita, S., Fabritius, T., Yasuno, Y., 2008. Quantitative retinal-blood flow measurement with three-dimensional vessel geometry determination using ultrahigh-resolution Doppler optical coherence angiography. Optics Letters 33, 836–838.

Merchant, S.N., Rosowski, J.J., 2010. Acoustic and mechanics of the middle ear. In: Gulya, A.J., Minor, L.B., Poe, D. (Eds.), Glasscock-Shambaugh Surgery of the Ear. Shelton, Ct., People's Medical Publishing House, USA, pp. 49–72.

Nakajima, H.H., Pisano, D.V., Roosli, C., Hamade, M.A., Merchant, G.R., Mahfoud, L., Halpin, C.F., Rosowski, J.J., Merchant, S.N., 2012. Comparison of ear-canal reflectance and umbo velocity in patients with conductive hearing loss: a preliminary study. Ear and Hearing 33, 35–43.

Nakajima, H.H., Ravicz, M.E., Merchant, S.N., Peake, W.T., Rosowski, J.J., 2005a. Experimental ossicular fixations and the middle ear's response to sound: evidence for a flexible ossicular chain. Hearing Research 204, 60–77.

Nakajima, H.H., Ravicz, M.E., Rosowski, J.J., Peake, W.T., Merchant, S.N., 2005b. Experimental and clinical studies of malleus fixation. Laryngoscope 115, 147–154.

Nguyen, C.T., Jung, W., Kim, J., Chaney, E.J., Novak, M., Stewart, C.N., Boppart, S.A., 2012. Noninvasive in vivo optical detection of biofilm in the human middle ear. Proceedings of the National Academy of Sciences of the United States of America 109, 9529–9534.

Oh, W.Y., Vakoc, B.J., Shishkov, M., Tearney, G.J., Bouma, B.E., 2010. >400 kHz repetition rate wavelength-swept laser and application to high-speed optical frequency domain imaging. Optics Letters 35, 2919–2921.

Parent, P., Allen, J.B., 2010. Time-domain "wave" model of the human tympanic membrane. Hearing Research 263, 152–167.

Pitris, C., Saunders, K.T., Fujimoto, J.G., Brezinski, M.E., 2001. High-resolution imaging of the middle ear with optical coherence tomography – a feasibility study. Archives of Otolaryngology-Head & Neck Surgery 127, 637–642.

Ravicz, M.E., Slama, M.C.C., Rosowski, J.J., 2010. Middle-ear pressure gain and cochlear partition differential pressure in chinchilla. Hearing Research 263, 16–25.

Rosowski, J.J., Cheng, J.T., Ravicz, M.E., Hulli, N., Hernandez-Montes, M., Harrington, E., Furlong, C., 2009. Computer-assisted time-averaged holograms of the motion of the surface of the mammalian tympanic membrane with sound stimuli of 0.4–25 kHz. Hearing Research 253, 83–96.

Rosowski, J.J., Dobrev, I., Khaleghi, M., Lu, W., Cheng, J.T., Harrington, E., Furlong, C., 2013. Measurements of three-dimensional shape and sound-induced motion of the chinchilla tympanic membrane. Hearing Research. in press.

Rosowski, J.J., Nakajima, H.H., Merchant, S.N., 2008. Clinical utility of laser-Doppler vibrometer measurements in live normal and pathologic human ears. Ear and Hearing 29, 3–19.

Shanks, J., Schohet, J., 2009. Tympanometry in clinical practice. In: Katz, J. (Ed.), Handbook of Clinical Audiology. Lippincott Williams & Wilkins, Philadelphia, pp. 157–188.

Subhash, H.M., Anh, N.H., Wang, R.K.K., Jacques, S.L., Choudhury, N., Nuttall, A.L., 2012. Feasibility of spectral-domain phase-sensitive optical coherence tomography for middle ear vibrometry. Journal of Biomedical Optics 17, 060505.

Tuck-Lee, J.P., Pinsky, P.M., Steele, C.R., Puria, S., 2008. Finite element modeling of acousto-mechanical coupling in the cat middle ear. Journal of the Acoustical Society of America 124, 348–362.

Vrettakos, P.A., Dear, S.P., Saunders, J.C., 1988. Middle-ear structure in the chinchilla – a quantitative study. American Journal of Otolaryngology 9, 58–67.

Wada, H., Ando, M., Takeuchi, M., Sugawara, H., Koike, T., Kobayashi, T., Hozawa, K., Gemma, R., 2002. Vibration measurement of the tympanic membrane of guinea pig temporal bones using time-averaged speckle pattern interferometry. Journal of the Acoustical Society of America 111, 2189–2199.

Yun, S.H., Tearney, G.J., de Boer, J.F., Iftimia, N., Bouma, B.E., 2003. High-speed optical frequency-domain imaging. Optics Express 11, 2953–2963.

Yun, S.H., Tearney, G.J., Vakoc, B.J., Shishkov, M., Oh, W.Y., Desjardins, A.E., Suter, M.J., Chan, R.C., Evans, J.A., Jang, I.K., et al., 2006. Comprehensive volumetric optical microscopy in vivo. Nature Medicine 12, 1429–1433.

(Supplementary Information)

Simultaneous 3D imaging of sound-induced motion of the eardrum and middle ear ossicles

Ernest W. Chang[a,b], Jeffrey T. Cheng[c,d], Christof Röösli[c,d,e], James B. Kobler[f,g], John J. Rosowski[c,d,h,1], Seok Hyun Yun[a,h,i,1]

[a]Wellman Center for Photomedicine, Massachusetts General Hospital, 50 Blossom St., Boston, MA 02114.

[b]Department of Biomedical Engineering, Boston University, Boston, MA.

[c]Eaton-Peabody Laboratory, Massachusetts Eye and Ear Infirmary, Boston, MA.

[d]Department of Otology and Laryngology, Harvard Medical School, Boston, MA.

[e]Department of Otorhinolaryngology, Head and Neck Surgery, University Hospital Zürich, Switzerland.

[f]Department of Surgery, Harvard Medical School, Boston, MA.

[g]Center for Laryngeal Surgery and Voice Rehabilitation, Massachusetts General Hospital, MA.

[h]Harvard-MIT Health Science and Technology, Cambridge, MA.

[i]Department of Dermatology, Harvard Medical School, Boston, MA.

*Correspondence should be addressed to: syun@hms.harvard.edu (S.H.Y.) or John_Rosowski@meei.harvard.edu (J.J.R.)

Content

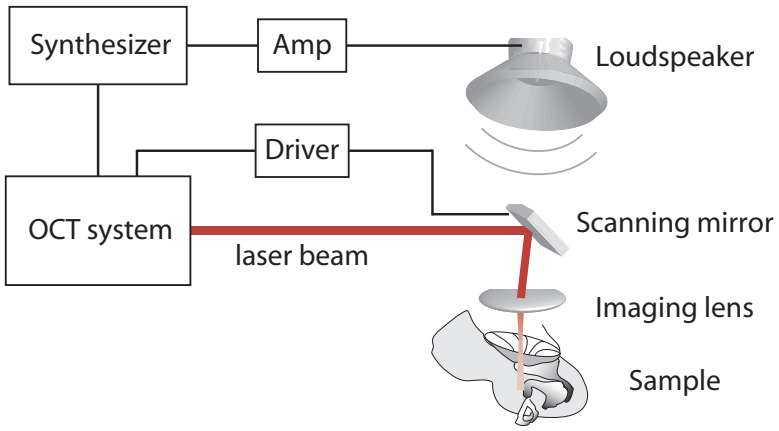

Fig. S1: Schematic of the experimental setup. OCT imaging system is built around a home-built swept laser with a polygon-mirror based laser filter. The near-infrared OCT beam is controlled by the XY scanning galvanometer-mounted mirror and an objective lens focuses the steered light onto the sample. Monotone sinusoidal signals from the synthesizer are further amplified with an audio amplifier. The amplified signal is directed to a loudspeaker near the sample. A two-channel 10 MS/s digitizer (National Instruments) is used to acquire the interferometric signals. A single clock generated from the computer data acquisition (DAQ) serves as a master clock to synchronize the polygon driver, galvanometer driver, signal synthesizer, and the data acquisition to achieve high phase sensitivity.

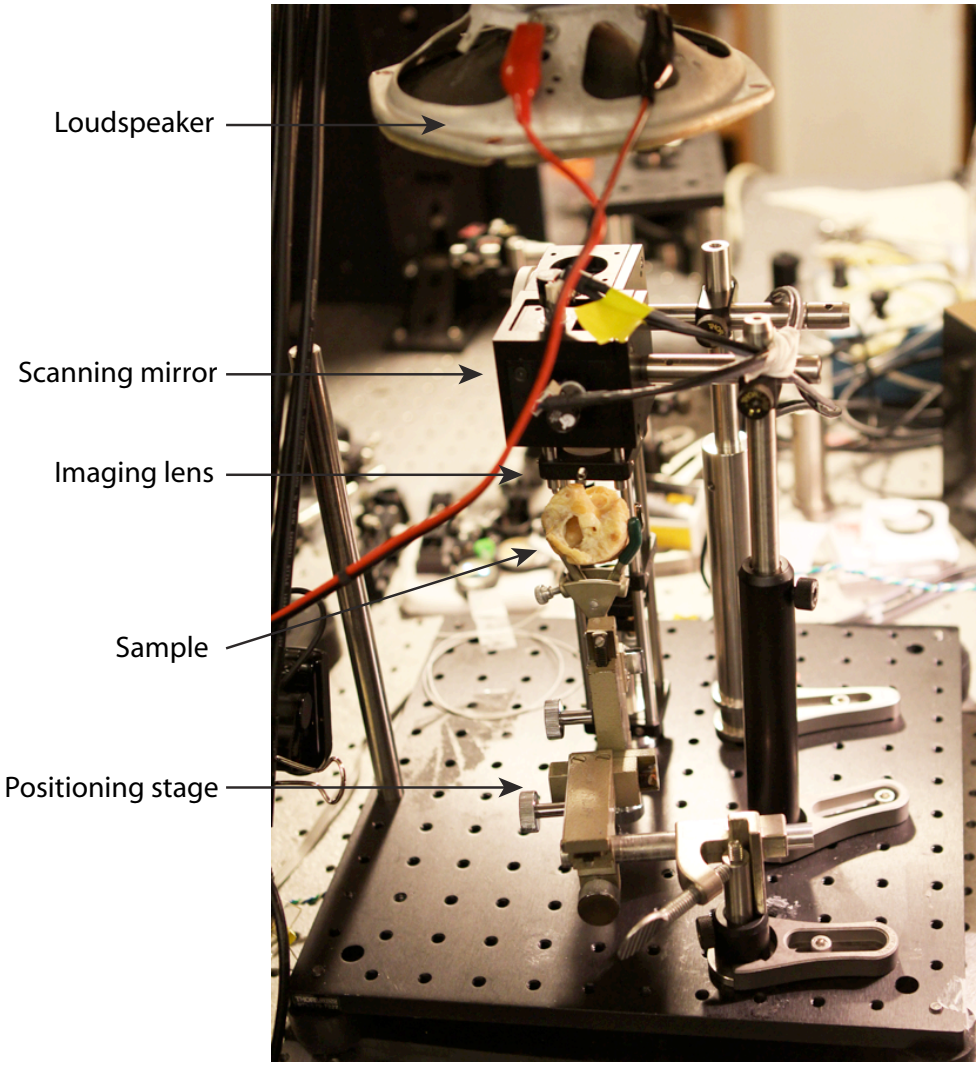

Fig. S2: Picture of the sample stage setup.

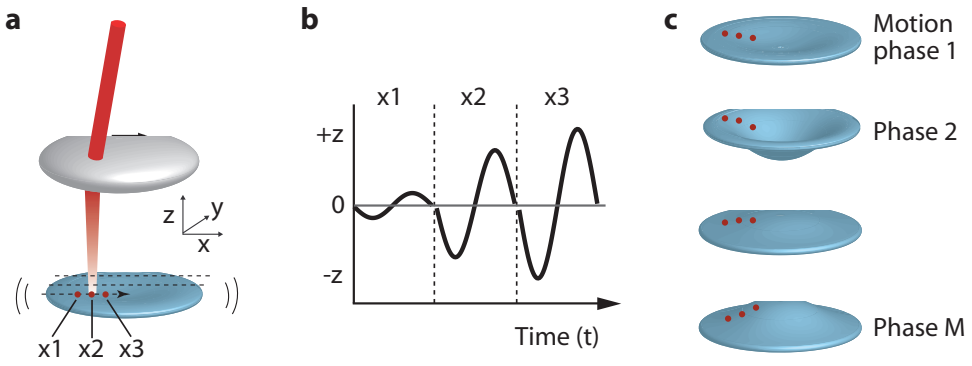

Fig. S3: Illustration of data acquisition and processing for vibrography. (a) The OCT probe beam (red) is focused on a sample (membrane) that vibrates at a frequency, *f*. The imaging beam is parked at a specific location (e.g. x1) for a single vibration cycle, and then moved to the next location (x2) for the next cycle. This process is repeated until the entire area is scanned. The number of A-lines, M, acquired at each location is given by the ratio of the sound frequency divided by the A-line rate. *F*; that is, M = *mod*(F/f). (b) Time-trace A-line images of the sample surface, acquired at three sequential locations, x1, x2, and x3. (c) Reconstructed vibrography images of the sample. A total M snapshot images are reproduced. For example, for f=2 kHz and F=20 kHz, M=10.

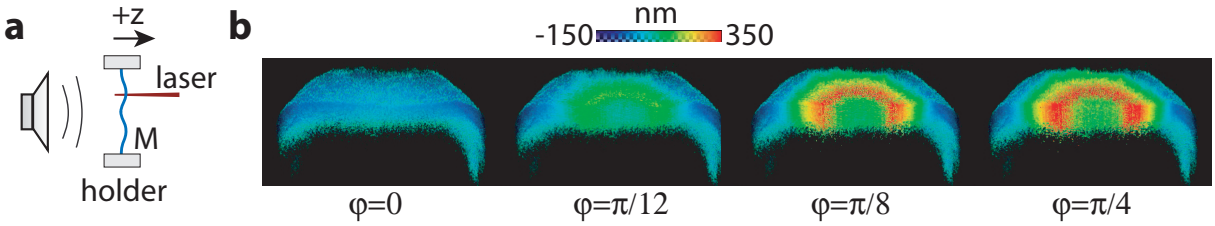

Fig. S4: Vibrography of a rubber membrane. (a) Setup. (b) 3D images of sound-driven motion at four phases. At the sound frequency of 800 Hz, the third axially symmetric membrane mode was excited, as indicated by the maximum in amplitude located between the center and the rim. The membrane was digitally bisected revealing uniform movement of the rubber across the cross-section. See **Video S1**.

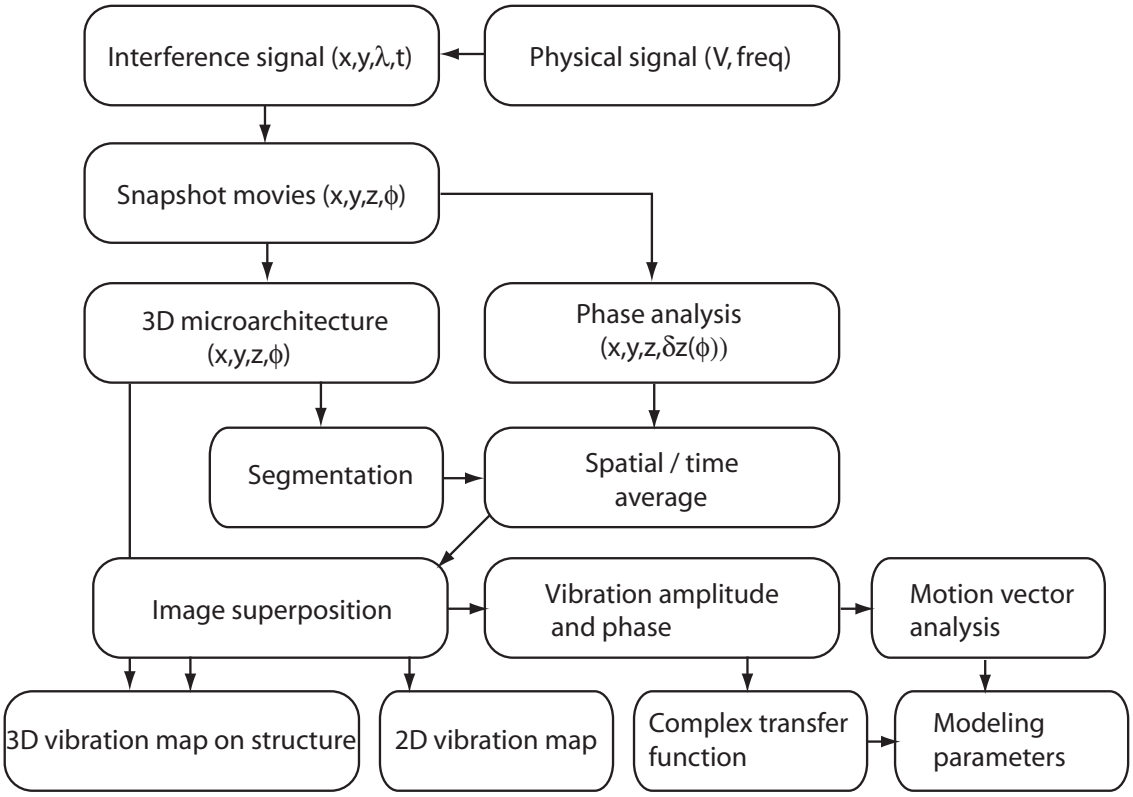

Fig. S5: Flowchart of data processing and analysis. Vibration snapshots, spatial amplitude and phase maps of objects are extracted from the OCT interferometry data. Each step is described in the Supplementary Method at the end of this supplementary document.

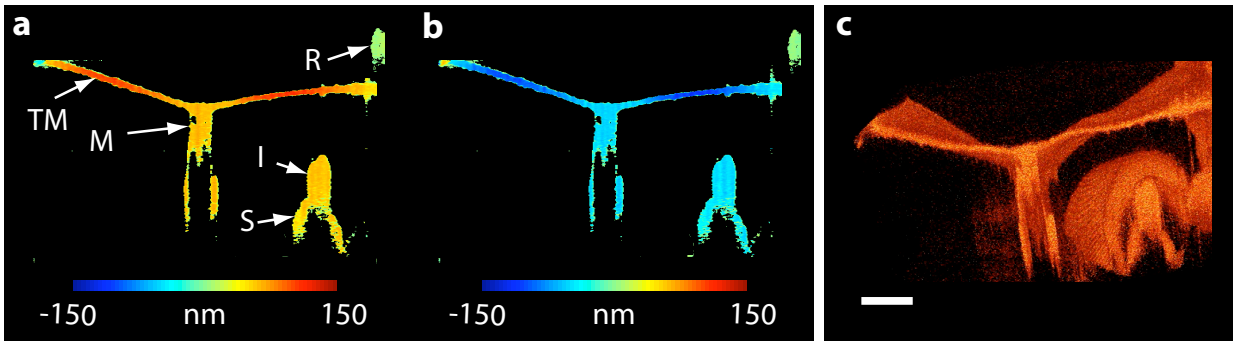

Fig. S6: (a, b) Cross-sectional vibration snapshots of chinchilla middle ear at two opposing phases of motion (See **Video S2a**). The stimulus frequency was 800 Hz. TM: tympanic membrane, M: handle of malleus, I: distal portion of incus, S: crus of stapes, R: stationary bony remnant. (c) 3D vibrography image at 1000 kHz, where the displacement was exaggerated to aid visualization (See **Video S2b**). Scale bar, 1 mm. For comparison, see the color-encoded vibrography images in **Video S2c** (1000 Hz) and **Video S2d** (500 Hz).

(Supplementary Information)

Simultaneous 3D imaging of sound-induced motion of the eardrum and middle ear ossicles

Ernest W. Chang[a,b], Jeffrey T. Cheng[c,d], Christof Röösli[c,d,e], James B. Kobler[f,g], John J. Rosowski[c,d,h,1], Seok Hyun Yun[a,h,i,1]

[a]Wellman Center for Photomedicine, Massachusetts General Hospital, 50 Blossom St., Boston, MA 02114.

[b]Department of Biomedical Engineering, Boston University, Boston, MA.

[c]Eaton-Peabody Laboratory, Massachusetts Eye and Ear Infirmary, Boston, MA.

[d]Department of Otology and Laryngology, Harvard Medical School, Boston, MA.

[e]Department of Otorhinolaryngology, Head and Neck Surgery, University Hospital Zürich, Switzerland.

[f]Department of Surgery, Harvard Medical School, Boston, MA.

[g]Center for Laryngeal Surgery and Voice Rehabilitation, Massachusetts General Hospital, MA.

[h]Harvard-MIT Health Science and Technology, Cambridge, MA.

[i]Department of Dermatology, Harvard Medical School, Boston, MA.

*Correspondence should be addressed to: syun@hms.harvard.edu (S.H.Y.) or John_Rosowski@meei.harvard.edu (J.J.R.)

Content

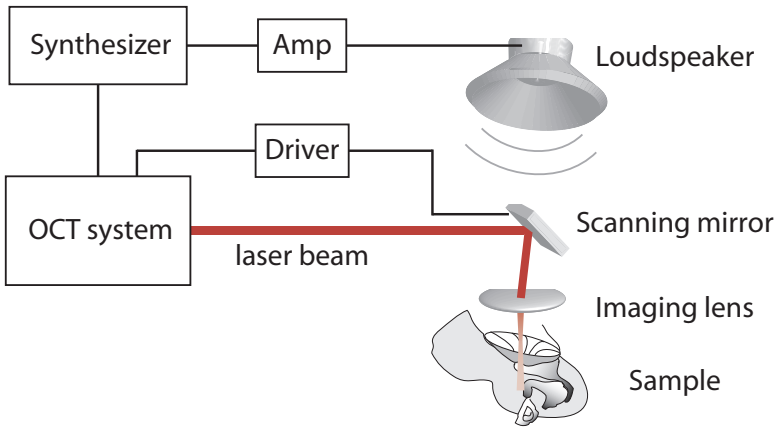

Fig. S1: Schematic of the experimental setup. OCT imaging system is built around a home-built swept laser with a polygon-mirror based laser filter. The near-infrared OCT beam is controlled by the XY scanning galvanometer-mounted mirror and an objective lens focuses the steered light onto the sample. Monotone sinusoidal signals from the synthesizer are further amplified with an audio amplifier. The amplified signal is directed to a loudspeaker near the sample. A two-channel 10 MS/s digitizer (National Instruments) is used to acquire the interferometric signals. A single clock generated from the computer data acquisition (DAQ) serves as a master clock to synchronize the polygon driver, galvanometer driver, signal synthesizer, and the data acquisition to achieve high phase sensitivity.

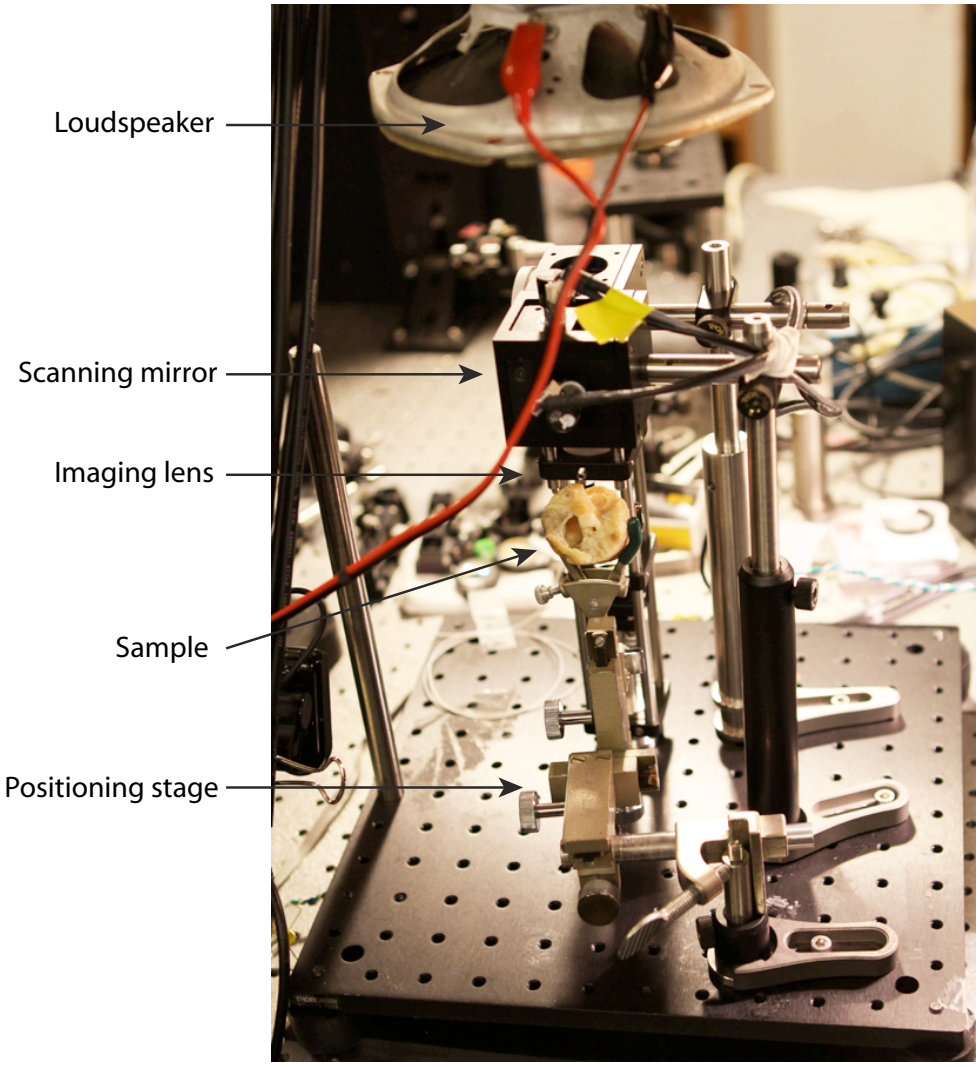

Fig. S2: Picture of the sample stage setup.

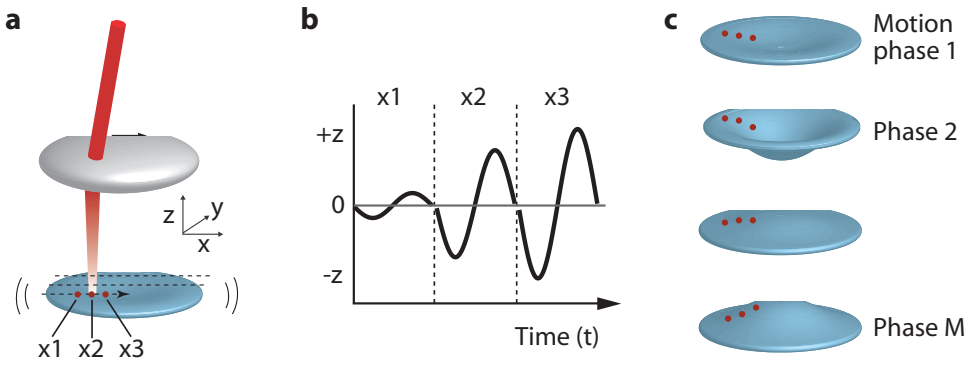

Fig. S3: Illustration of data acquisition and processing for vibrography. (a) The OCT probe beam (red) is focused on a sample (membrane) that vibrates at a frequency, *f*. The imaging beam is parked at a specific location (e.g. x1) for a single vibration cycle, and then moved to the next location (x2) for the next cycle. This process is repeated until the entire area is scanned. The number of A-lines, M, acquired at each location is given by the ratio of the sound frequency divided by the A-line rate. *F*; that is, M = *mod*(F/f). (b) Time-trace A-line images of the sample surface, acquired at three sequential locations, x1, x2, and x3. (c) Reconstructed vibrography images of the sample. A total M snapshot images are reproduced. For example, for f=2 kHz and F=20 kHz, M=10.

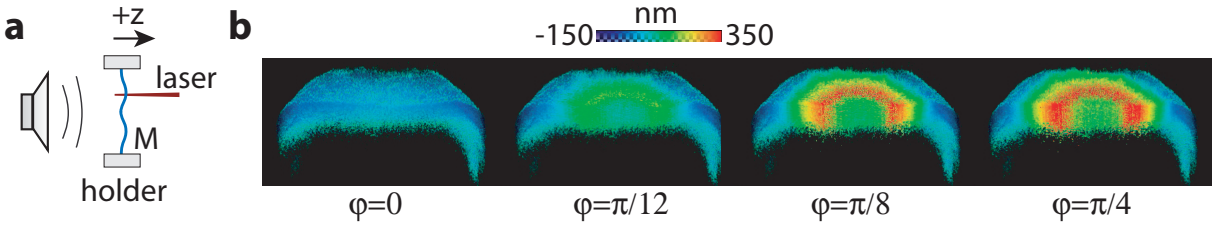

Fig. S4: Vibrography of a rubber membrane. (a) Setup. (b) 3D images of sound-driven motion at four phases. At the sound frequency of 800 Hz, the third axially symmetric membrane mode was excited, as indicated by the maximum in amplitude located between the center and the rim. The membrane was digitally bisected revealing uniform movement of the rubber across the cross-section. See **Video S1**.

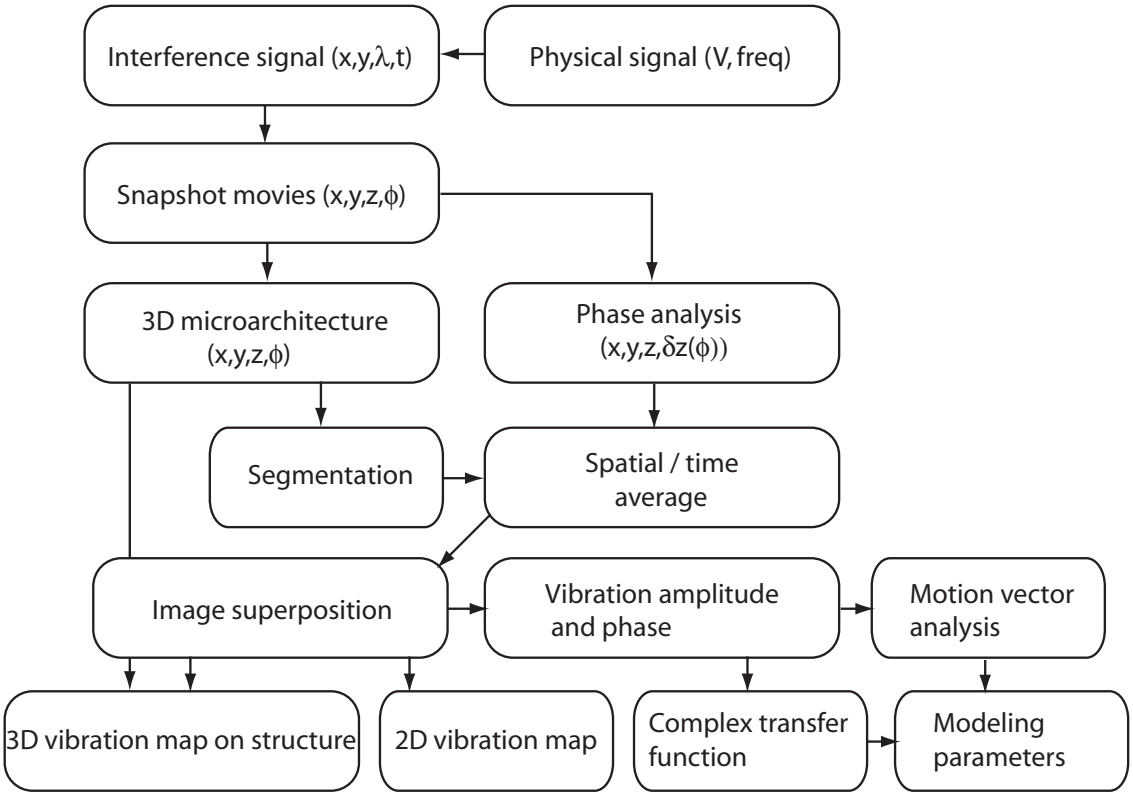

Fig. S5: Flowchart of data processing and analysis. Vibration snapshots, spatial amplitude and phase maps of objects are extracted from the OCT interferometry data. Each step is described in the Supplementary Method at the end of this supplementary document.

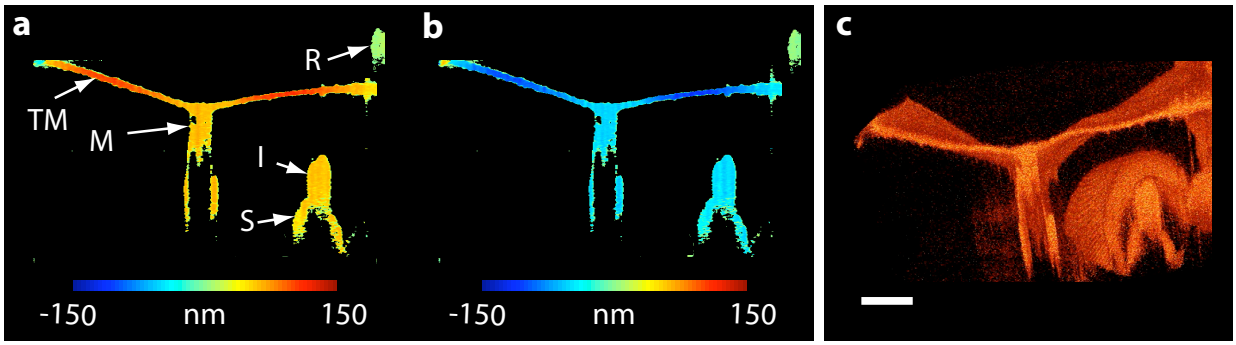

Fig. S6: (a, b) Cross-sectional vibration snapshots of chinchilla middle ear at two opposing phases of motion (See **Video S2a**). The stimulus frequency was 800 Hz. TM: tympanic membrane, M: handle of malleus, I: distal portion of incus, S: crus of stapes, R: stationary bony remnant. (c) 3D vibrography image at 1000 kHz, where the displacement was exaggerated to aid visualization (See **Video S2b**). Scale bar, 1 mm. For comparison, see the color-encoded vibrography images in **Video S2c** (1000 Hz) and **Video S2d** (500 Hz).

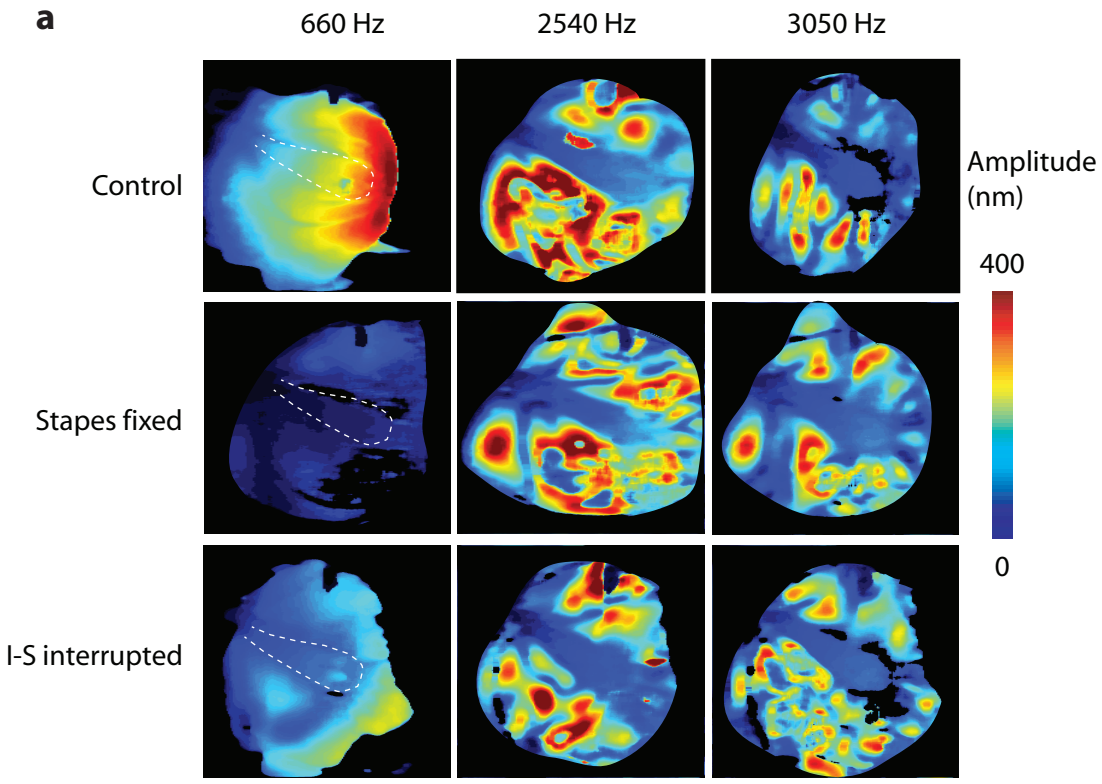

Fig. S7: (a) Vibration amplitude maps. The dashed line indicates the outline of the manubrium. As the sound frequency increases, more vibration nodes appear.

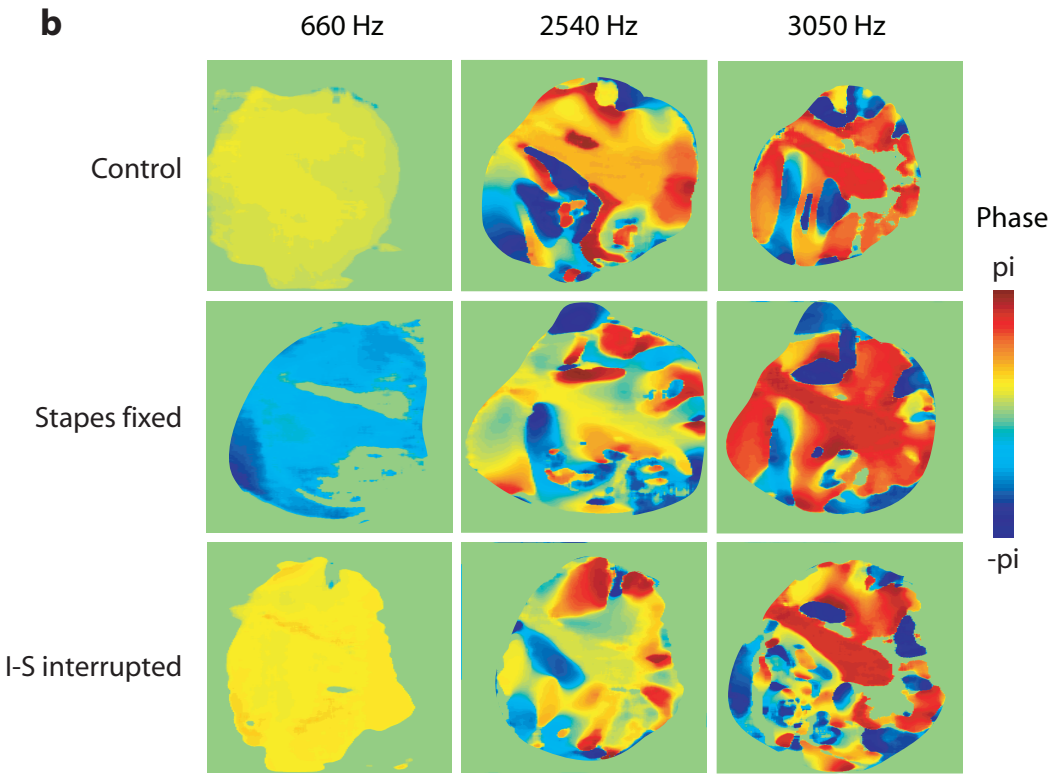

Fig. S7 (*Continued from the previous page*): (b) Phase maps corresponding to the amplitude maps in (a) in the previous page.

Supplementary Methods

OCT system: Frequency-domain OCT enables high-resolution optically-sectioned imaging by measuring the interference signal between light scattered from the tissue and a reference as a function of wavelength. Fourier analysis of the interference signal gives optically-sectioned signals at all detectable depths. Lateral resolution is determined from the NA of the imaging lens. Axial resolution is determined by the bandwidth of the swept laser source. Measuring the phase delays in the interference signals gives nanometer-scale resolution of motion in the direction parallel to the imaging beam.

The optical frequency domain imaging (OFDI) system was based on a home-built wavelength swept source [1]. A multi-functional data acquisition board (DAQ; PCI 6115, National Instruments) was used to acquire interference data at 10 MS/s and control the polygon filter (Lincoln Lasers) of the laser source to generate A-line rates of 15-20 kHz. The tuning range of the laser was 130 nm around a mean wavelength of 1280 nm. The DAQ board also produced an analog output (16 bit) to control a two-axis galvanometer beam scanner (6210H, Cambridge Technologies) and provided a trigger signal to the function generator. By generating all the control signals from the internal time-base clock (20 MHz) of the DAQ board, we achieved synchronization among data acquisition, beam scanning, and phase of the sound stimulus. Data were acquired along the X and Y dimensions at 10-20 μm intervals across a transverse field of 5-10 mm.

Physical signal: The frequency of the driving monotone sinusoidal waveform was set at an integer fraction of the A-line rate (15-20 kHz), so that a number of A-lines were acquired during each cycle of excitation signal. The beam is moved after the completion of individual vibration cycles. When the XY raster scans over the regions of interest in the sample were completed, A-line profiles acquired at the same phase of the oscillation were grouped to produce “snapshots” [2, 3, 4] or time-resolved vibrographs of the sample.

Signal and image processing: The following data processing procedures were used (see flowchart in Fig. S5).

> ***Snapshot data***: The time-resolved complex parameters of signal amplitude and phase are calculated via Fourier analysis of the raw optical scattering data. The resulting information is rearranged to generate 3D snapshots at different phases across the vibratory cycle.

3D micro-architecture: The magnitude of the scattering signal was used to produce time-independent three-dimensional magnitude scattering datasets with isotropic pitch in X and Y dimensions. These datasets were saved in log-scale as 8-bit tiff images. A 3D visualization software platform (Amira, Visage Imaging) was used to inspect the image stacks in 3D.

Thresholding and segmentation: Thresholding was applied to filter out features with signal-to-noise ratios lower than 25 to 30 dB. For segmentation of the tympanic membrane, the threshold was set to half the maximum scattering magnitude for each A-line (Fig. S8).

Phase analysis (motion): The OCT derived optical phase angle, ψ, can be expressed as $\psi(t) = \Delta\psi\ sin(2\pi ft)+\psi_n$, where $\Delta\psi = 4\pi/\lambda*\delta z$ is the optical phase amplitude corresponding to the amplitude of motion δz (in nanometer), λ is the center wavelength of the swept laser, f is the vibration frequency, and ψ_n is the intrinsic phase noise given by $<\delta\psi_n>^2=1/(2*SNR)$, where SNR is the signal-to-noise ratio in the intensity of the interference signal [2, 5]. This phase angle can be extracted from the complex raw data with Fourier analysis and is subsequently rearranged to give snapshot images. Now each phase resolved snapshot image has the format of (x, y, z, $\delta z(\phi)$). These datasets were used to derive displacement (nm) of the sample in the z-dimension (parallel to the imaging beam).

Spatial/Time average: Both segmented structural data and motion data can be averaged spatially and temporally. Spatiotemporal averaging of the motion data increases the motion sensitivity by $N^{1/2}$ where N is the number of spatially or temporally averaged pixels. In this work, spatial averaging was used when analyzing the motion of specific region of interest (ROI).

***Image superposition*:** The displacement data was mapped onto the thresholded 2D and 3D structures at each phase in the motion cycle and visualized using Amira.

***Vibration amplitude and phase*:** Volumetric vibration amplitude and phase were calculated from the Fourier analysis superposed 4D dataset (x, y, z, $\delta z(\phi)$). The amplitude and phase maps give motion vector analysis (phase map) and complex transfer function (both amplitude and phase) used as parameters for modeling.

References

1. Yun SH, Tearney GJ, de Boer JF, Iftimia N & Bouma BE (2003) High-speed optical frequency-domain imaging. *Opt. Express* 11: 2953-2963.
2. Chang, EW, Kobler, JB & Yun SH (2012) Subnanometer optical coherence tomographic vibrography. *Opt. Lett.* 37: 3678-3680.
3. Chang EW, Kobler JB & Yun SH (2011) Triggered optical coherence tomography for capturing rapid periodic motion. *Sci. Rep.* 1: 49.
4. Kobler JB, Chang EW, Zeitels SM & Yun SH (2010) Dynamic imaging of vocal fold oscillation with four-dimensional optical coherence tomography. *Laryngoscope* 120: 1354-1362.
5. Vakoc BJ, Lanning R.M, Tyrrell JA *et al*. (2009) Three-dimensional microscopy of the tumor microenvironment in vivo using optical frequency domain imaging. *Nat. Med.* 15: 1219-1223.

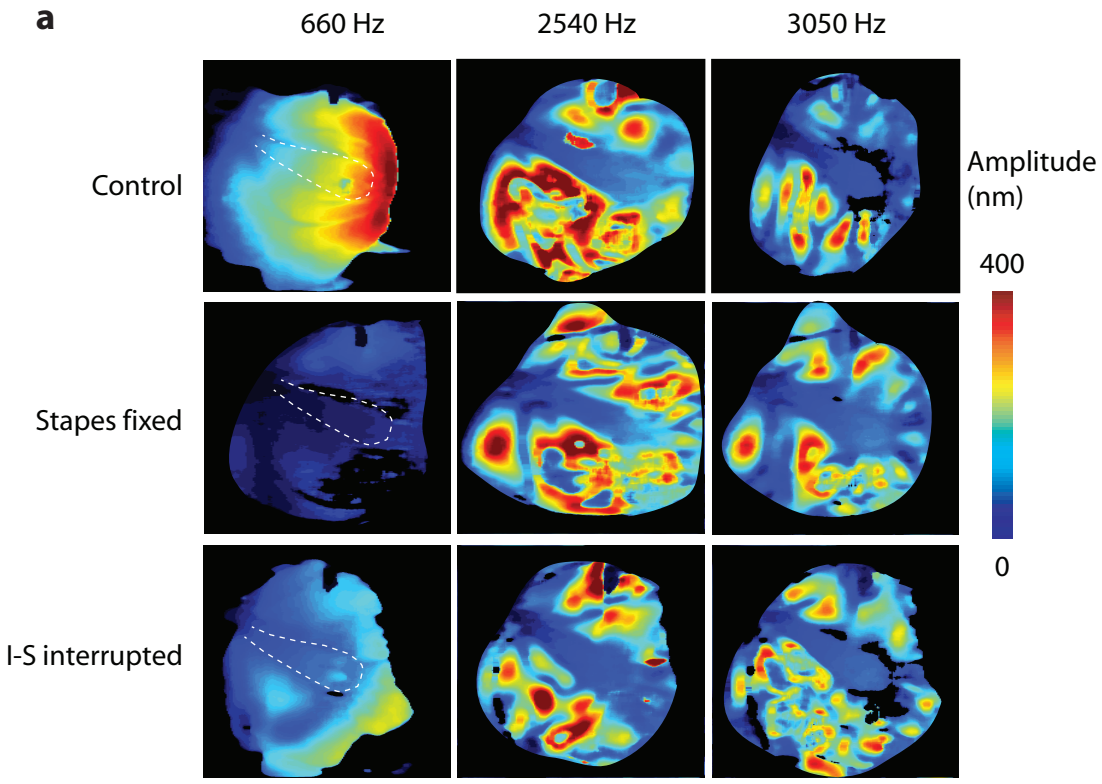

Fig. S7: (a) Vibration amplitude maps. The dashed line indicates the outline of the manubrium. As the sound frequency increases, more vibration nodes appear.

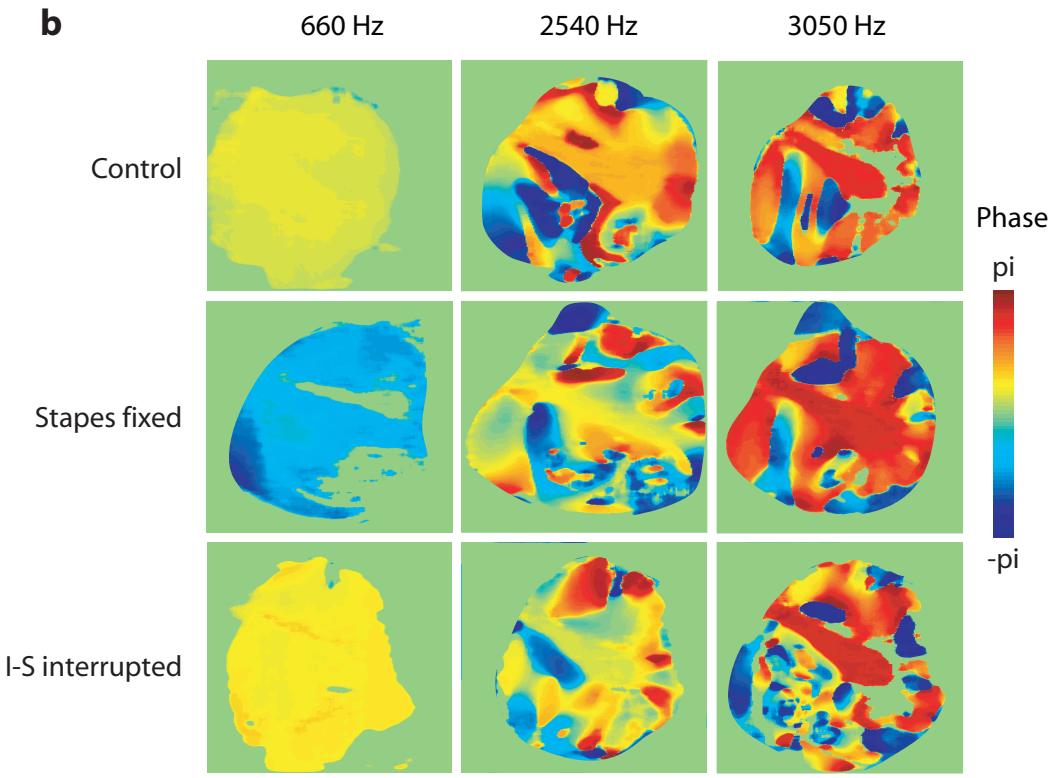

Fig. S7 (*Continued from the previous page*): (b) Phase maps corresponding to the amplitude maps in (a) in the previous page.

Supplementary Methods

OCT system: Frequency-domain OCT enables high-resolution optically-sectioned imaging by measuring the interference signal between light scattered from the tissue and a reference as a function of wavelength. Fourier analysis of the interference signal gives optically-sectioned signals at all detectable depths. Lateral resolution is determined from the NA of the imaging lens. Axial resolution is determined by the bandwidth of the swept laser source. Measuring the phase delays in the interference signals gives nanometer-scale resolution of motion in the direction parallel to the imaging beam.

The optical frequency domain imaging (OFDI) system was based on a home-built wavelength swept source [1]. A multi-functional data acquisition board (DAQ; PCI 6115, National Instruments) was used to acquire interference data at 10 MS/s and control the polygon filter (Lincoln Lasers) of the laser source to generate A-line rates of 15-20 kHz. The tuning range of the laser was 130 nm around a mean wavelength of 1280 nm. The DAQ board also produced an analog output (16 bit) to control a two-axis galvanometer beam scanner (6210H, Cambridge Technologies) and provided a trigger signal to the function generator. By generating all the control signals from the internal time-base clock (20 MHz) of the DAQ board, we achieved synchronization among data acquisition, beam scanning, and phase of the sound stimulus. Data were acquired along the X and Y dimensions at 10-20 μm intervals across a transverse field of 5-10 mm.

Physical signal: The frequency of the driving monotone sinusoidal waveform was set at an integer fraction of the A-line rate (15-20 kHz), so that a number of A-lines were acquired during each cycle of excitation signal. The beam is moved after the completion of individual vibration cycles. When the XY raster scans over the regions of interest in the sample were completed, A-line profiles acquired at the same phase of the oscillation were grouped to produce “snapshots” [2, 3, 4] or time-resolved vibrographs of the sample.

Signal and image processing: The following data processing procedures were used (see flowchart in Fig. S5).

> ***Snapshot data***: The time-resolved complex parameters of signal amplitude and phase are calculated via Fourier analysis of the raw optical scattering data. The resulting information is rearranged to generate 3D snapshots at different phases across the vibratory cycle.

3D micro-architecture: The magnitude of the scattering signal was used to produce time-independent three-dimensional magnitude scattering datasets with isotropic pitch in X and Y dimensions. These datasets were saved in log-scale as 8-bit tiff images. A 3D visualization software platform (Amira, Visage Imaging) was used to inspect the image stacks in 3D.

Thresholding and segmentation: Thresholding was applied to filter out features with signal-to-noise ratios lower than 25 to 30 dB. For segmentation of the tympanic membrane, the threshold was set to half the maximum scattering magnitude for each A-line (Fig. S8).

Phase analysis (motion): The OCT derived optical phase angle, ψ, can be expressed as $\psi(t) = \Delta\psi\ sin(2\pi ft)+\psi_n$, where $\Delta\psi = 4\pi/\lambda*\delta z$ is the optical phase amplitude corresponding to the amplitude of motion δz (in nanometer), λ is the center wavelength of the swept laser, f is the vibration frequency, and ψ_n is the intrinsic phase noise given by $<\delta\psi_n>^2=1/(2*SNR)$, where SNR is the signal-to-noise ratio in the intensity of the interference signal [2, 5]. This phase angle can be extracted from the complex raw data with Fourier analysis and is subsequently rearranged to give snapshot images. Now each phase resolved snapshot image has the format of (x, y, z, $\delta z(\phi)$). These datasets were used to derive displacement (nm) of the sample in the z-dimension (parallel to the imaging beam).

Spatial/Time average: Both segmented structural data and motion data can be averaged spatially and temporally. Spatiotemporal averaging of the motion data increases the motion sensitivity by $N^{1/2}$ where N is the number of spatially or temporally averaged pixels. In this work, spatial averaging was used when analyzing the motion of specific region of interest (ROI).

***Image superposition*:** The displacement data was mapped onto the thresholded 2D and 3D structures at each phase in the motion cycle and visualized using Amira.

***Vibration amplitude and phase*:** Volumetric vibration amplitude and phase were calculated from the Fourier analysis superposed 4D dataset (x, y, z, $\delta z(\phi)$). The amplitude and phase maps give motion vector analysis (phase map) and complex transfer function (both amplitude and phase) used as parameters for modeling.

References

1. Yun SH, Tearney GJ, de Boer JF, Iftimia N & Bouma BE (2003) High-speed optical frequency-domain imaging. *Opt. Express* 11: 2953-2963.
2. Chang, EW, Kobler, JB & Yun SH (2012) Subnanometer optical coherence tomographic vibrography. *Opt. Lett.* 37: 3678-3680.
3. Chang EW, Kobler JB & Yun SH (2011) Triggered optical coherence tomography for capturing rapid periodic motion. *Sci. Rep.* 1: 49.
4. Kobler JB, Chang EW, Zeitels SM & Yun SH (2010) Dynamic imaging of vocal fold oscillation with four-dimensional optical coherence tomography. *Laryngoscope* 120: 1354-1362.
5. Vakoc BJ, Lanning R.M, Tyrrell JA *et al*. (2009) Three-dimensional microscopy of the tumor microenvironment in vivo using optical frequency domain imaging. *Nat. Med.* 15: 1219-1223.